Analytical Methods

ROYAL SOCIETY OF CHEMISTRY

PAPER

View Article Online
View Journal

Cite this: DOI: 10.1039/d6ay00130k

Optimisation of through-vial Raman analysis of turbid samples by modelling the Raman intensity-depth decay response

Vasundhara Tyagi,[a] Alexander G. Shard,[a] Ryan T. Coones,[a] Dimitrios Tsikritsis,[a] Enya Murray,[a] Elizabeth Legge,[a] Caterina Minelli[a] and Natalie A. Belsey*[ab]

Raman spectroscopy enables non-destructive chemical analysis and can be performed through-vial, eliminating air exposure. However, signal attenuation arises from refraction, absorption, and scattering within the sample, while distortions and spectral interference from the vial further degrade signal collection and data quality. This study investigates depth-dependent Raman intensity decay in polystyrene (PS) particle suspensions as a model for turbid liquids and proposes a framework of equations and approaches based on Mie scattering theory and the Beer–Lambert law to predict Raman intensity decay in a range of samples. Experimental validation was performed using aqueous suspensions containing 495 nm, 350 nm, and 200 nm PS particles using an 830 nm laser, with Raman spectra acquired at incremental depths. Peak areas corresponding to PS, water, and glass were recorded. Mie theory was used to model the UV-visible extinction response, yielding estimated absorbance and, combined with the intensity decay due to refraction established from non-turbid samples, Raman intensity decay lengths. Estimated decay lengths for PS and water showed good agreement with experimental values, typically within 20%. This framework enables rapid optimisation of focal depth and consistent comparison between samples and experiments for quantitative through-container Raman analysis in pharmaceuticals, materials science, and nanotechnology.

Received 23rd January 2026
Accepted 11th March 2026

DOI: 10.1039/d6ay00130k

rsc.li/methods

Introduction

Raman spectroscopy (RS) is an analytical technique used to study vibrational, rotational, and other low-frequency modes in a diverse range of sample types including medical, food, forensics, pharmaceutical and materials research.[1,2] RS relies on the phenomenon of the Raman effect, where a molecule inelastically scatters photons from an incident beam.[3] The Raman shift represents the change in wavelength of the scattered light compared to the incident light and can be of two types: (i) Stokes: when the scattered light has lower energy (longer wavelength) than the incident light. Stokes scattering is typically associated with the most intense Raman lines and corresponds to a molecular transition to an excited vibrational state, and (ii) anti-Stokes: in which the scattered light has higher energy (shorter wavelength) than the incident light and corresponds to a molecular transition to a lower energy vibrational state.

One of the key advantages of Raman spectroscopy is its ability to allow chemical detection and quantification of an analyte non-destructively. The configuration of the incident laser source and detection system allows measurements to be performed through containers such as glass vials, by directing an external laser to illuminate the sample within.[4,5] These measurements support a wide range of applications – including in pharmaceuticals,[6] forensics,[7] and security[8] – where preserving the sample or protecting against exposure is essential, either because only a small quantity of the analyte is available or because the toxicity of the sample is high or unknown. A common challenge for many of these applications is the rapid loss of Raman signal within the sample volume due to light absorption[9] and elastic scattering by particles in the dispersion. This is more significant for larger particles and often constrains the location of the measurement to within few tens of microns of the sample container. However, the strong Raman signal from, for example, the glass container that can overwhelm the signal collected from within the vial and overlap with the analyte peaks of interest.[10] Complex optical geometries of laser-illumination and photon-detection may be used such as spatially offset Raman,[10,11] to minimize or eliminate the glass signal,[10] in the conventional backscattering confocal Raman spectroscopy scheme, peak fitting methods are often necessary to quantify the Raman signal of interest from deeper into the

[a]Chemical and Biological Sciences Department, National Physical Laboratory, Hampton Road, Teddington, Middlesex, TW11 0LW, UK. E-mail: natalie.belsey@npl.co.uk
[b]School of Chemistry & Chemical Engineering, University of Surrey, Guildford, GU2 7XH, UK

vial where the signal overlaps with background signals from the vial itself in addition to the decrease in intensity due to the diffusion of photons in the medium.

Another challenge for such measurements is optimising the focusing parameters for layered (through-container) samples containing materials of differing refractive indices. Such samples will reduce Raman signal intensity and decrease axial resolution with increasing penetration depth, making it challenging for the Raman analyst to choose optimum conditions for reliable qualitative and quantitative measurements. To avoid signal attenuation, depth resolution should be maintained close to the nominal value. This can be achieved by avoiding laser refraction by using an immersion objective coupled with a fluid that matches the refractive index of the sample,[12,13] or by analysing a serial cross section of the sample.[14] Neither of which are practical for through-vial Raman measurements of a composite sample, therefore modelling and fitting methods can facilitate data interpretation in such measurements.

Over the past three decades, some effort has been devoted to interpreting Raman depth profiles in dry objective systems. For thin samples, Tabaksblat *et al.* employed a geometrical optics framework to characterise the intensity variation within transparent samples in the conjugate back-focal plane while ignoring diffraction effects,[15] De Grauw *et al.* refined the model by considering a Gaussian beam profile instead of a spherical beam, leading to a Lorentzian Raman intensity axial distribution for a thin polystyrene film.[16] For thicker planar interfaces, Everall developed a simple model to quantify the distortions encountered by the laser-illuminated spot as it undergoes refraction at the air/sample interface in accordance with Snell's law, demonstrating that the focal volume of illumination substantially exceeds the theoretical diffraction limit (several tens of micrometres) and the axial depth resolution may also degrade by several orders of magnitude relative to its nominal diffraction-limited value, with the extent of deterioration increasing with imaging depth.[12,17,18] Baldwin and Batchelder's model incorporated a pinhole in the collection pathway to the model, which reduced the focal volume, and highlighted that collection efficiency markedly decreases with increasing focus depth.[19] Further refinement by Sourisseau *et al.* using a vectorial electromagnetic framework, incorporated diffraction effects in their computational model – including off-axis incident intensity distributions, diffraction integrals for confocal aperture transmission, and phase aberrations – accurately predicting through-plane confocal Raman responses at varying focus depths.[20] Others have experimentally validated and refined the models, Tomba *et al.* experimentally validated the simpler models by incorporating on-axis laser intensity profiles and renormalising the depth-resolution curves using independently measured collection efficiencies which significantly enhanced the agreement between experimental data and model predictions,[21] they also proposed a regularised deconvolution approach to partition the sample thickness into multiple planes, reconstructing the overall emission intensity by combining the contribution from each.[22] More recently, Chakraborty and Kahan extended the modelling and experimental validation of total intensity depth profiles in surface and volume emitting samples.[23] Maier and Bohm presented a similar computational model that deconvoluted the system's point spread function from ideal sample profiles, accounting for refractive index mismatches and subsurface intensity loss, the model was able to accurately predict axial resolution and its decay with depth for layer thickness estimation when the sample's refractive index is known.[24]

Recently Giovannini *et al.* presented a comprehensive theoretical perspective on the challenges in modelling Raman data in complex environments, such as solutions, highlighting the importance of understanding solute–solvent interactions, phase space and molecular geometry.[25] However, there is a lack of modelling validation studies focused on turbid colloidal systems containing micro- or nanoparticles.

In this paper, we use polystyrene (PS) nanoparticle colloids contained in a borosilicate glass vial – a typical container used in analytical sciences, to address the experimental and modelling challenges mentioned above through different approaches – (i) for experimental data, using direct least squares analysis to extract the PS, the container (glass) and the medium (water) signals at each incremental depth, and (ii) modelling the UV-visible and Raman intensity decay of PS particles dispersions to understand and ultimately predict the loss of Raman signal in turbid samples in a container. Modelled UV-visible and Raman data has been validated with experimental data. Successful modelling of Raman signal decay in turbid samples will enable analysts to adjust optical focusing to obtain more accurate quantitative measurements and to understand the limited sampling depth available in scattering samples.

Materials and methods

Materials

PS nanoparticles (3000 Series Nanosphere™ Size Standards) with a diameter of 200 nm, 350 nm and 495 nm with reported concentration of 1% w/v solids, were purchased from Fisher Scientific (UK) and were stored refrigerated at 4 °C. Dilutions were performed volumetrically in ultrapure water (resistivity = 18.2 MΩ cm), into 2 mL clear borosilicate glass vials (Merck KGaA, Darmstadt, Germany). Prior to measurements, samples were sonicated in an ultrasonic bath for 10 minutes, and very gently shaken immediately before measurements to minimize agglomeration and sedimentation.

Raman spectroscopy

Raman spectroscopy measurements were performed with an inVia Qontor spectrometer (Renishaw plc, UK) with a 50×, 0.5 NA long working distance objective lens (Leica Microsystems Ltd, Germany). Raman spectra were acquired with an 830 nm laser, a power at the sample of (92.0 ± 1.6) mW and a theoretical diffraction limited line profile spot size of ~2 μm in *x*-axis, ~7 μm in *y*-axis, and >10 μm in *z*-axis. Depth profile measurements were performed on glass vials containing PS suspensions, where a spectrum was acquired at 10 μm depth intervals, starting from 200 μm above the top of the vial and moving down into the

suspension. At each position the spectrum was acquired with 2 accumulations of 30 s. Data analysis was performed in WiRE 5.3 for removal of spikes caused by cosmic rays, baseline subtraction and peak fitting, which were performed in this order, as required. While the use of a confocal aperture would more effectively block out-of-focus scattering, its use in the present study was precluded due to the substantial signal reduction for PS and water, which would have necessitated significantly longer acquisition times.

For least squares analysis, individual components were extracted by performing depth scans of a water only sample in a vial using the same parameters described above. Individual glass components were extracted for each sample from within the depth series (around 140 μm within the glass wall). Individual PS components were arithmetically obtained by subtracting the isolated glass and water components. Least squares analysis was performed using a custom Python script, using Python 3.11.11 version and scipy.optimize module. Graphs were produced in Microsoft Excel and Origin 2025.

UV-visible spectroscopy

UV-visible extinction responses were acquired using matched quartz cuvettes (Hellma, semi-micro quartz Suprasil™) with an optical path length of 10 mm using a Cary 60 UV-visible spectrophotometer (Agilent, Santa Clara, CA). Samples were diluted volumetrically.

Mie scattering code

Mie theory was used to model the interaction of light with spherical nanoparticles and predict optical extinction spectra for direct comparison with experimental UV-visible measurements.[26–28] Model UV-visible spectra were generated using a custom Python script based on the open-source library miepython,[29] which provides an implementation of the analytical Mie solution to Maxwell's equations.[29] This approach enables the calculation of electromagnetic scattering by a homogeneous, isotropic spherical particle suspended in a non-absorbing medium. The script computes wavelength-dependent scattering and absorption efficiencies, which were used to simulate the spectral response of particles under study.

Results and discussion

Modelling of Raman and UV-visible extinction response

Raman depth profiling fitting. For the analysis of the Raman intensity depth profiles, curves were fitted to the data to measure experimental decay lengths (the distance over which light intensity decreases by $1/e$), and therefore the distance within which a measurement should be acquired. The shape of the Raman intensity profiles from the composite samples illustrated in this study (Fig. 1) were modelled by considering the container (glass vial) and content (PS and water) separately. The glass vial was considered first, to calculate the position of the inner glass wall, and the depth resolution at that interface.

We find that the depth profile of the glass, taken from the intensity of the glass vial peak in the Raman spectra, can be fitted with a model function which considers the two interfaces of air–glass and glass–PS suspension. The approach is based upon the practical, empirical description of Maier and Böhm.[24] Resolution functions at each interface are assumed to be described by a Lorentzian distribution and intensity decays by exponentials. We describe the shape of the intensity trace of glass by the combination of two cumulative Lorentzian resolution functions, where the first interface is modelled by one function representing increasing intensity, and the second interface modelled by another function which can be subtracted from the first to represent the decrease in intensity. The resulting intensity trace can be described by:

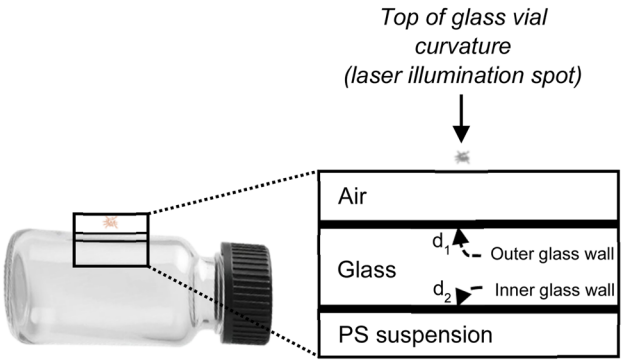

Fig. 1 Illustration of sample configuration used in this study.

$$I_g = \frac{I_g^{ref}}{\pi}\left[\arctan\left(\frac{d-d_1}{\gamma_1}\right) - \arctan\left(\frac{d-d_2}{\gamma_2}\right)\right] \quad (1)$$

where d is the depth into the sample, d_1 and d_2 are, respectively, the apparent upper and lower boundaries of the wall of the glass vial and γ_1 and γ_2 are the half-width at half-maximum of the two Lorentzian profiles at the interfaces. These values and the intensity reference value I_g^{ref} are found by least squares fitting of eqn (1) to the experimental data. No significant drop in intensity is expected through the wall of the glass vial, therefore no exponential decay function is included in the fit, which is in good agreement with the results. The apparent thickness of the glass ($d_2 - d_1$) was found to be within 5% of 0.50 mm, as expected.

Raman depth profiles of PS and water (experimental peak centred at 1002 and 1638 cm^{-1} respectively) were fitted with an exponential decay described by

$$I_x = I_x^{ref}\frac{1}{\pi}\left[0.5 + \arctan\left(\frac{d-d_2}{\gamma_2}\right)\right]\left[\exp\left(\frac{d_2-d}{\lambda_x}\right) + I_x^{BG}\right] \quad (2)$$

where x = PS or water. d_2 and γ_2 are obtained from the fit to the glass signal and the intensity reference, I_x^{ref}, decay length, λ_x, and background intensity, I_x^{BG}, are found from the least squares fit of eqn (2) to the experimental data of either PS or water. The PS and water data were only fitted within the region of the solution when $d > d_2$. The purpose of these fits is to obtain the characteristic length of intensity decay within the sample to compare with the expected decay lengths from the Beer–Lambert law.

UV-visible extinction. Although acquiring experimental UV-visible extinction data is straightforward with commercially available instruments, the wavelength range is limited by the light source and detector of the instrument. In this case, the laser wavelength used for Raman analysis (830 nm) was outside the range of the UV-visible spectrometer. We overcome this limitation by using theoretical UV-visible extinctions at the incident source and scattered wavelengths to model the Raman decay profiles of the spherical PS particles and validate them within the UV-visible spectrometer range.

When interacting with incident light, PS particles are predominantly scattering in nature and exhibit low absorption at the Raman source and scattered wavelengths, and therefore the Raman decay length is primarily influenced by light penetration depth. Mie theory provides a comprehensive description of light scattering by spherical particles, offering exact solutions to Maxwell's equations in the context of particle sizes comparable to the wavelength of incident light.[30,31]

The Mie solution begins with the assumption of a plane-polarized electromagnetic wave incident upon a spherical particle with a well-defined diameter, D and complex refractive index, $m(\lambda) = n(\lambda) + ik(\lambda)$, where λ is the wavelength of light, and n and k are the wavelength-dependent real and imaginary parts of the refractive index, respectively. The surrounding medium was assumed to have a refractive index, n_{med}, and the size parameter, x, is defined as:

$$x = \frac{\pi D n_{med}}{\lambda} \quad (3)$$

Given the size parameter and relative refractive index ($m_{rel} = m_p/n_{med}$), where m_p is the complex refractive index of the particle, we used the widely available miepython module to calculate the Mie coefficients a_n and b_n which arise from the series expansion of the scattered and internal fields in terms of spherical Bessel and Hankel functions.[29] This ensures continuity of the tangential electric and magnetic fields that arise at the particle boundary as described by Maxwell's equations. Further details on miepython are provided in the materials section. From these coefficients, the wavelength-dependent Mie efficiencies were computed.

Extinction efficiency is calculated according to eqn (4):[32,33]

$$Q_{ext} = \frac{2}{x^2}\sum_{n=1}^{N}(2n+1) \times \mathbb{R}(a_n + b_n) \quad (4)$$

Q_{ext} quantifies the total attenuation of the light due to both scattering and absorption phenomena by a spherical particle relative to its geometric cross-section. Here, x is the size parameter defined in eqn (3). $\mathbb{R}(a_n + b_n)$ describes the real part of the sum of the Mie coefficients, and N is the number of terms considered in the series. We note that Q_{ext} strongly depends on λ through the size parameter x and the Mie coefficients a_n and b_n which are also a function of the size parameter, as well as through other parameters of the terms of the Bessel and Hankel functions.

These quantities could then be used to calculate model UV-visible extinction spectra using the Beer–Lambert law in its natural logarithm form, as in eqn (5), to calculate the effective absorbance, A, at a given wavelength. Similar works have been done elsewhere for nanoparticles of various materials and sizes.[34–36]

$$A = 0.3411 r^2 Q_{ext} C L \quad (5)$$

where r is the particle radius, Q_{ext} is the extinction efficiency, C is the number concentration of the particles by volume, and L is the optical path length of the light through the cuvette.

Conversion of UV-visible extinction to Raman decay response. The absorbance values were then converted into Raman decay lengths using the Beer–Lambert law:

$$A = \log_{10}\left(\frac{I_0}{I}\right) \quad (6)$$

where A = absorbance, I_0 = intensity of incident light, I = intensity of transmitted light.

Eqn (7) describes how light intensity decays exponentially as it passes through a material of thickness d, where Λ is the characteristic decay length which represents the distance over which light intensity decreases by $1/e$.

$$I = I_0 \exp\left(\frac{-d}{\Lambda}\right) \quad (7)$$

From eqn (6) and (7):

$$\Lambda = \frac{d}{\ln(10)A} \quad (8)$$

The overall Raman decay length was then estimated by combining the different sources of decay along the pathway, using the harmonic sum described in eqn (9). This is equivalent to the summation of effective cross sections for each of the processes:

$$\frac{1}{\Lambda_1} = \frac{1}{\Lambda_{in}} + \frac{1}{\Lambda_{out}} + \frac{1}{\Lambda_{water}} \quad (9)$$

where Λ_1 = overall effective Raman decay length, Λ_{in} = decay length of the incident light (before Raman scattering), Λ_{out} = decay length of the scattered Raman light (after Raman scattering) and Λ_{water} accounts for additional loss of intensity in the non-turbid medium. The latter decay of intensity arises from refraction effects and loss of focus but can be adequately described with an exponential decay. In this work, Λ_{water} is found from Raman intensity depth profiles of particle-free water.

Confocal Raman depth measurements

Fig. 2 shows the Raman spectra of 350 nm (2 g L^{-1}) diameter PS particles in water acquired at different depths above, within and below the glass vial wall. Peaks of interest include: 1794 cm^{-1} corresponding to the glass vial, a broad peak at 1638 cm^{-1} corresponding to the O–H vibrational bending mode from water,[37] peaks at 1584 cm^{-1} and 1602 cm^{-1} corresponding to the C=C and ring skeletal stretch respectively from PS.[38,39]

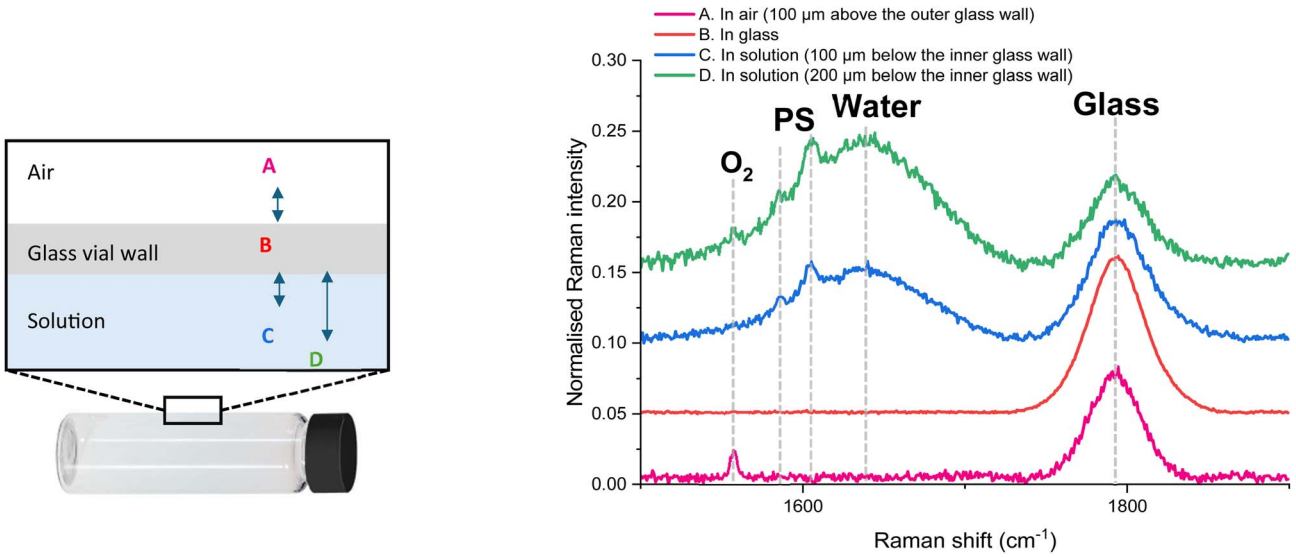

Fig. 2 Normalised Raman spectrum of 350 nm diameter PS particle suspension in water contained within a glass vial at four different depths (A) 100 μm above the outer glass wall (in air), (B) within the glass wall, (C) 100 μm and (D) 200 μm below the inner glass wall. Raman traces are offset for clarity.

A peak at 1557 cm^{-1} is assigned to gaseous oxygen[40] in atmospheric air within the instrument chamber. A near infrared 830 nm incident laser was chosen to avoid fluorescence signal originating from the borosilicate glass vial. These spectra demonstrate the overwhelming extent to which the signal from the container (glass) dominates the spectra – while the water

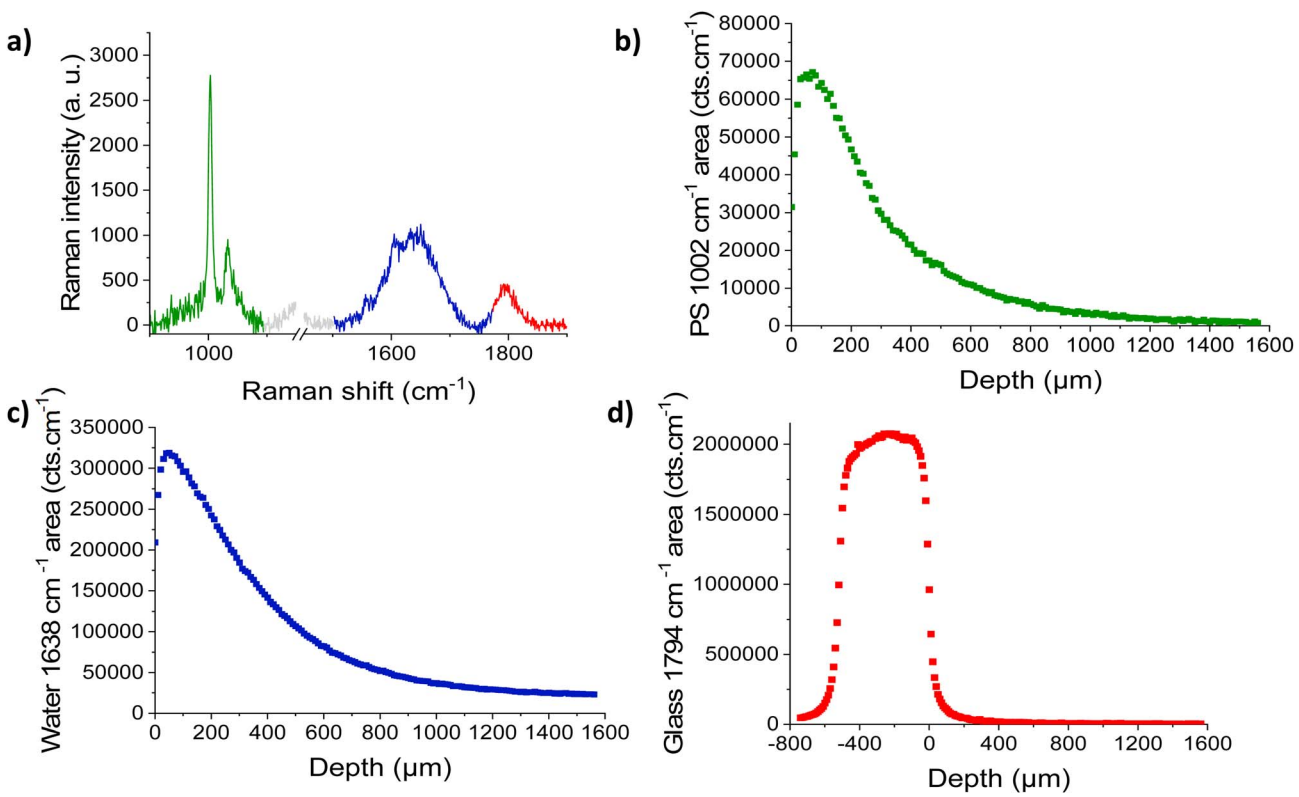

Fig. 3 (a) Raman spectra of 350 nm (2 g L^{-1}) PS in water (2 g L^{-1}) acquired at a depth of 400 μm from the glass–water interface with the characteristic PS, water and glass peaks shown in green, blue and red after removal of spikes caused by cosmic rays and baseline subtraction, (b) peak area of the peak centred at 1002 cm^{-1} corresponding to PS as a function of depth (0 μm = glass–water interface), (c) peak area of the peak centred at 1638 cm^{-1} corresponding to water as a function of depth (0 μm = glass–water interface), (d) peak area of the peak centred at 1794 cm^{-1} corresponding to glass as a function of depth (0 μm = glass–water interface).

and PS peaks are detected at depths of 100 μm (C) and 200 μm (D) below the inner glass surface, corresponding to their actual physical locations, glass signals appear throughout the analysis depth, including in regions where it is not physically present, such as in air (A) and solution (C, D). To address this issue and effectively separate the PS and water signals from the glass and from each other, direct least squares analysis was applied independently at each of the 231 depth increments. Raman spectra were acquired from 200 μm above the top wall of the glass vial to approximately 1600 μm into the vial. Fig. 3a shows one of the Raman spectra from the depth series measurement of 350 nm PS particles (2 g L^{-1}), and the area of the characteristic PS (green), water (blue) and glass (red) peaks with maxima at 1002 cm^{-1}, 1638 cm^{-1} and 1794 cm^{-1} respectively. Fig. 3b–d show the intensity of each component as a function of depth, where the glass–water interface is taken as the reference position.

PS and water signal areas reached a maximum at a depth of <100 μm inside the vial before decaying exponentially. The glass signal exhibited no noticeable loss of signal over the 500 μm wall thickness.

Fig. 4a shows the area of the PS peak centred at 1002 cm^{-1}, at increasing depths for 495 nm, 350 nm and 200 nm (2 g L^{-1} and 4 g L^{-1}) within the glass vial. Assuming that the deterioration of axial resolution due to refraction was similar for all samples, the decay of Raman signal with depth is due to absorption and scattering of incident and collected light along the optical path as size and concentration of particles increases. Doubling the particle mass concentration from 2 g L^{-1} to 4 g L^{-1} resulted in increases of 1.6-, 1.7-, and 1.5-fold in the maximum PS signal (expressed as area) for particles measuring 495 nm, 350 nm, and 200 nm, respectively. These increases were lower than expected, because the Raman signal is expected to scale linearly with concentration suggesting a two fold increase should have occurred. One possible explanation is sedimentation of particles, which may have reduced the effective PS signal.

Fig. 4b shows the area of the water peak centred at 1638 cm^{-1} for samples containing different size and concentrations of PS particles, and water in the absence of PS (in cyan). Larger and more concentrated particles showed an exponential loss of water signal due to scattering, while decay of water signal in samples with smaller 200 nm sized particles looked closer to the profile of water alone. Due to the small losses observed in the water signal for 200 nm size particles, water signal could also be used to normalise the PS signal to account for optical losses with depth and measurement conditions (Fig. 4c) to obtain consistent results at all depths. This approach has previously been used for signal correction in the relative quantification of polymeric particles in water.[4,41] However, for larger particles, the signal collection for water was too poor to be used as a correction reference, indicating the importance of understanding particle size and the resulting turbidity dependent Raman signal decay behaviour.

In-depth experimental studies such as the one mentioned in this work that are crucial to devise quantitative studies are resource-intensive (>10 hours acquisition time for each sample), therefore a modelling approach would be valuable for Raman analysts to faster-optimize their measurements.

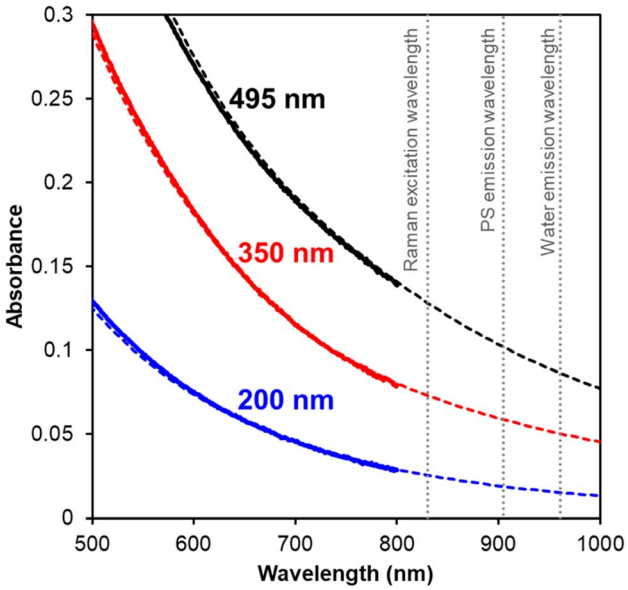

Fig. 5 Average of experimentally obtained absorbance ($n = 3$) shown in solid line and modelled absorbance in dashed line for (a) 200 nm (blue), (b) 350 nm (red) and (c) 495 nm (black) sized PS particles (4 g L^{-1}).

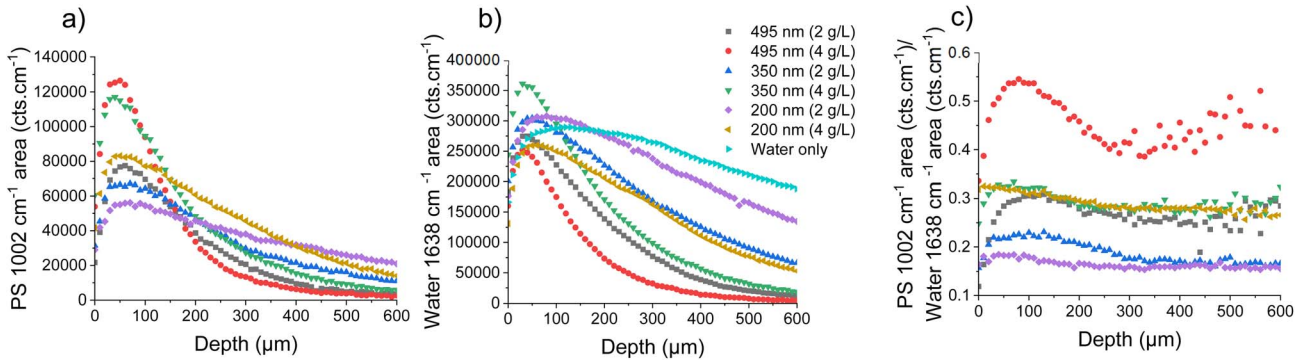

Fig. 4 Raman peak areas of 495 nm, 350 nm and 200 nm PS particles (2 g L^{-1} and 4 g L^{-1}) for peak centre (a) 1002 cm^{-1} corresponding to PS, (b) 1638 cm^{-1} corresponding to water, and (c) ratio of PS and water peak areas.

A simple approach would be to measure the UV-visible extinction at the wavelengths used in the Raman experiment. However, this is not always feasible for the type of samples used by analysts where extraction and dilution can change the nature of the samples. In this case, the wavelengths used in Raman were outside the range of most UV-visible spectrometers and therefore an alternative approach was used. To model the Raman signal of transparent PS particles, the first step involved calculating their theoretical extinction which would enable the estimation of extinction behaviour of PS and water at their Raman emission wavelengths (905 nm for PS and 961 nm for water). The calculated extinction spectra were validated within the range of a UV-visible spectrometer. Fig. 5 shows the extinction spectra of PS particles experimentally measured using UV-visible spectroscopy (solid lines) and theoretically modelled using Mie theory (dashed lines). The experimental data is an average of three replicates. The results demonstrated a good agreement showing that Mie theory effectively describes the optical behaviour of these particles. The vertical lines display the incident laser wavelength (830 nm) and emission wavelengths of PS and water.

Fig. 6 shows representative results of 350 nm (4 g L^{-1}) PS particles in water obtained by fitting of experimental Raman spectra with individual components using least squares analysis as described in the methods (dots), and the intensity depth profiles fitted with curves described in the modelling section (in solid line) for glass (Fig. 6a), PS (Fig. 6b) and water (Fig. 6c). The residual distribution can be found in supplementary information and indicated a good fit between the two data sets.

The Raman decay lengths were obtained by fitting the experimentally obtained intensities with curves described in the modelling section. The resulting values are compared to theoretically estimated decay lengths calculated according to eqn (9).

Table 1 shows the estimated and experimentally obtained Raman decay lengths of the different size and concentrations of PS nanoparticles. These lengths describe the effective distance from the glass–water interface over which PS and water Raman signal can be collected with high confidence. Experimental values have an estimated uncertainty of around 10%, arising from the fitting uncertainty, instrumental noise and sample dependent effects. A good agreement was observed between the estimated and experimental decay length data sets with a typical agreement within ~20%.

The loss of Raman signal from PS with depth was both size and concentration dependent – the experimental decay lengths decreased as the particle size or concentration increased. The overall decrease in Raman intensity with increasing particle size

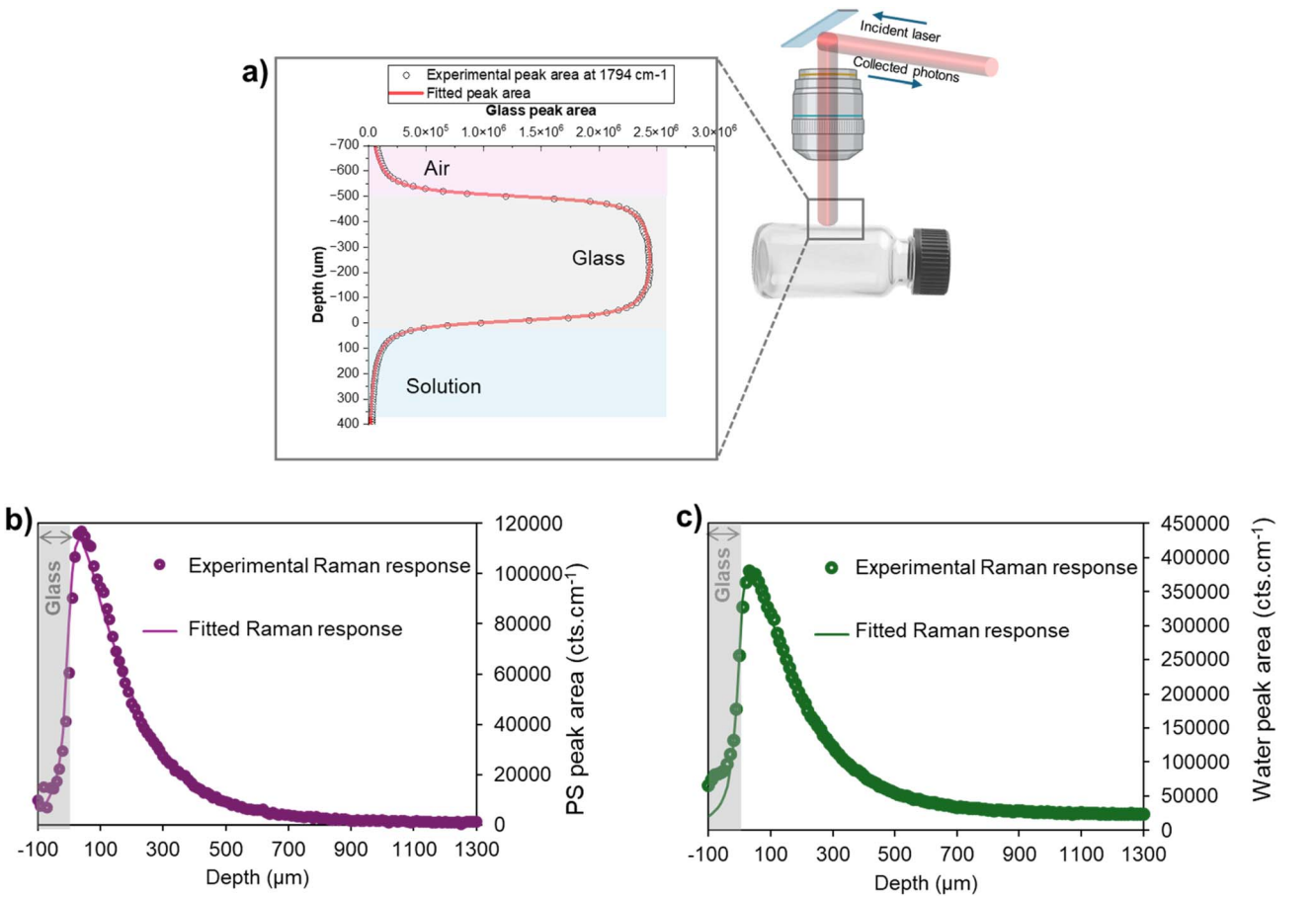

Fig. 6 Experimentally obtained and fitted Raman response of 350 nm PS particles in water for (a) glass peak area of peak centred at 1794 cm^{-1}, (b) PS peak area of peak centred at 1002 cm^{-1} and (c) water peak area of peak centred at 1638 cm^{-1}.

Table 1 Estimated *versus* experimental Raman decay lengths (the distance over which light intensity decreases by 1/*e*) of 200 nm, (2.4 g L^{-1}), 350 nm (2.4 g L^{-1}) and 495 nm (2.4 g L^{-1}) size PS particles. The decay length of the water signal intensity in pure water is 1032 μm. The experimental decay lengths have an estimated 10% uncertainty

		Estimated decay length (μm)		Experimental decay length (μm)		Experimental/estimated decay length	
Diameter (nm)	Concentration (g L^{-1})	PS	Water	PS	Water	PS	Water
200	2	576	597	483	561	0.84	0.94
350	2	308	322	281	330	0.91	1.03
495	2	202	214	184	167	0.91	0.78
200	4	399	420	294	330	0.74	0.79
350	4	181	191	159	167	0.88	0.88
495	4	112	119	114	112	1.02	0.94

has been previously documented in the literature,[42,43] with some exceptions.[43] In addition to the previously discussed axial resolution worsening with depth which may contribute to signal loss, another possible effect is the poorer signal collection compounded by the increased extinction as PS solution gets visibly more turbid when the particle size or concentration increases.

By understanding the distance over which the scattered light significantly loses intensity within the vial, Raman spectroscopy instrument users designing their particle detection and quantification experiment can determine the appropriate acquisition depth to maximize the signal of interest. This approach establishes a framework that enable to compare results and predict different samples and experiments. For example, application of the present approach enabled to predict Raman decay lengths of 711 μm for PS and 730 μm for water in suspensions containing 125 nm PS particles, consistent with the ~700 μm upper limit for reproducible measurements experimentally reported by Legge *et al.*[4] When sample dilution is not possible, Raman analysts can use this modelling approach to improve the data interpretation of depth-dependent Raman measurements in through-container measurements.

Overall, this approach provides a rapid way to predict how Raman signals weaken as they penetrate deeper into a sample by incorporating both confocal resolution effects and intensity decay due to scattering losses. Analysts can apply this knowledge to optimize their experimental parameters, ensuring optimum signal collection and awareness of the confounding factors such as background interference or signal loss due to optical limitations.

Limitations of this approach include prior knowledge about the refractive index, size and mass concentration of the particles. The size of the particles can be easily measured by methods such as dynamic light scattering or particle tracking analysis. The mass concentration can be measured by performing titration measurements to calibrate the Raman signal. Mie scattering also has limitations that affect its accuracy in real-world applications such as disregarding multiple scattering events, and assumptions including particles being perfect spheres, monodisperse and optically uniform, and the surrounding medium being non-absorbing and homogeneous, which may not reflect the actual conditions in a sample. For higher confidence, a greater number of experimental and theoretical replicates must be generated, and future work should extend these models to account for absorbing particles and other non-geometrical structural complexities, further enhancing the predictive capabilities and broadening the potential applications of this technique in diverse analytical scenarios. For example, Lu *et al.* have developed a method for correcting the self-absorption effect, such that the non-attenuated Raman spectrum can be recovered.[9]

Conclusions

In this study, we have investigated the depth-dependent Raman intensity decay in PS particle suspensions, focusing on the effects of scattering and depth losses within a glass vial. By applying Mie scattering theory and the Beer–Lambert law, we developed a predictive model for Raman signal attenuation in non-absorbing particulate systems using theoretical absorbance values of a single particle. As expected, the experimental results demonstrated a gradual decrease in Raman intensity with depth, with larger particles exhibiting greater signal attenuation due to increased scattering. The proposed fitting-based approach, which accounts for confocal resolution and scattering, exhibited excellent agreement with the experimental data, demonstrating a robust model for predicting Raman signal decay. The findings of this study can be used to bring consistency and comparability across different datasets and accelerate analysis for applications in fields like pharmaceuticals, materials science, and nanotechnology, where non-destructive, through-container analysis is essential. By refining the understanding of Raman signal attenuation in particle suspensions, this work facilitates more precise quantification and characterisation of materials in various media. However, limitations remain, particularly regarding the applicability of the model to light absorbing nanoparticles or more complex sample matrices.

Author contributions

V. T.: conceptualisation, data curation, formal analysis, supervision, investigation, methodology, project administration, software, validation, writing – original draft, writing – review & editing; A. S.: formal analysis, investigation, software, validation, writing – review & editing; R. C.: software, validation, writing – original draft, writing – review & editing; D. T.: methodology, writing – review & editing, E. M.: data curation, investigation; E. L.: formal analysis, writing – review & editing; C. M.: supervision, writing – review & editing; N. B.: conceptualization, supervision, funding acquisition, resources, project administration, writing – review & editing.

Conflicts of interest

Authors declare no conflict of interest.

Data availability

The data supporting this article have been included as part of the supplementary information (SI). Supplementary information is available. See DOI: https://doi.org/10.1039/d6ay00130k.

Acknowledgements

The authors acknowledge funding from the National Measurement System programme of the UK Department for Science, Innovation and Technology.

References

1 A. Orlando, *et al.*, A Comprehensive Review on Raman Spectroscopy Applications, *Chemosensors*, 2021, **9**(9), 262.
2 E. M. Suzuki and P. Buzzing, Applications of Raman spectroscopy in forensic science. I: Principles, comparison to infrared spectroscopy, and instrumentation, *Forensic Sci. Rev.*, 2018, **30**(2), 111–135.
3 C. V. Raman and K. S. Krishnan, A New Type of Secondary Radiation, *Nature*, 1928, **121**, 501–502.
4 E. J. Legge, *et al.*, Non-invasive quantitative chemical measurements of liposomal formulations using Raman spectroscopy, *RSC Pharm.*, 2025, **2**(2), 279–291.
5 R. L. McCreery, *et al.*, Noninvasive identification of materials inside USP vials with Raman spectroscopy and a Raman spectral library, *J. Pharm. Sci.*, 1998, **87**(1), 1–8.
6 E. Caudron, *et al.*, Identification of hematite particles in sealed glass containers for pharmaceutical uses by Raman microspectroscopy, *J. Pharm. Biomed. Anal.*, 2011, **54**(4), 866–868.
7 A. D. Burnett, *et al.*, A forensic case study: the detection of contraband drugs in carrier solutions by Raman spectroscopy, *Drug Test. Anal.*, 2011, **3**(9), 539–543.
8 G. Mogilevsky, *et al.*, Raman Spectroscopy for Homeland Security Applications, *Int. J. Spectro.*, 2012, **2012**(1), 808079.
9 L. Lu, *et al.*, Resonance Raman scattering of β-carotene solution excited by visible laser beams into second singlet state, *J. Photochem. Photobiol., B*, 2018, **179**, 18–22.
10 Y. Lee, *et al.*, Direct through-container Raman spectroscopic analyses of samples housed in glass and plastic containers: a review, *Appl. Spectrosc. Rev.*, 2023, **58**(7), 509–524.
11 N. Gupta, J. D. Rodriguez and H. Yilmaz, Through-container quantitative analysis of hand sanitizers using spatially offset Raman spectroscopy, *Commun. Chem.*, 2021, **4**(1), 126.
12 N. Everall, Confocal Raman Microscopy: Why the Depth Resolution and Spatial Accuracy Can Be Much Worse Than You Think, *Appl. Spectrosc.*, 2000, **54**, 1515–1520.
13 N. J. Everall, Modeling and Measuring the Effect of Refraction on the Depth Resolution of Confocal Raman Microscopy, *Appl. Spectrosc.*, 2000, **54**(6), 773–782.
14 T. Böhm, R. Moroni and S. Thiele, Serial section Raman tomography with 10 times higher depth resolution than confocal Raman microscopy, *J. Raman Spectrosc.*, 2020, **51**(7), 1160–1171.
15 R. Tabaksblat, R. J. Meier and B. J. Kip, Confocal Raman Microspectroscopy: Theory and Application to Thin Polymer Samples, *Appl. Spectrosc.*, 1992, **46**(1), 60–68.
16 C. De Grauw, *et al.*, Axial resolution of confocal Raman microscopes: Gaussian beam theory and practice, *J. Microsc.*, 1997, **188**(3), 273–279.
17 N. J. Everall, Confocal Raman microscopy: common errors and artefacts, *Analyst*, 2010, **135**(10), 2512–2522.
18 N. Everall, *et al.*, Optimizing Depth Resolution in Confocal Raman Microscopy: A Comparison of Metallurgical, Dry Corrected, and Oil Immersion Objectives, *Appl. Spectrosc.*, 2007, **61**(3), 251–259.
19 K. J. Baldwin and D. N. Batchelder, Confocal Raman Microspectroscopy through a Planar Interface, *Appl. Spectrosc.*, 2001, **55**(5), 517–524.
20 C. Sourisseau and P. Maraval, Confocal Raman microspectrometry: a vectorial electromagnetic treatment of the light focused and collected through a planar interface and its application to the study of a thin coating, *Appl. Spectrosc.*, 2003, **57**(11), 1324–1332.
21 J. P. Tomba, L. M. Arzondo and J. M. Pastor, Depth Profiling by Confocal Raman Microspectroscopy: Semi-empirical Modeling of the Raman Response, *Appl. Spectrosc.*, 2007, **61**(2), 177–185.
22 J. P. Tomba, M. de la Paz Miguel and C. J. Perez, Correction of optical distortions in dry depth profiling with confocal Raman microspectroscopy, *J. Raman Spectrosc.*, 2011, **42**(6), 1330–1334.
23 S. Chakraborty and T. F. Kahan, A model for interpreting depth profiles of confocal Raman measurements in reflective and transmitting materials, *J. Raman Spectrosc.*, 2019, **50**(11), 1763–1776.
24 M. Maier and T. Böhm, Modeling the Depth Resolution of Translucent Layers in Confocal Microscopy, *Small Sci.*, 2024, **4**(9), 2400120.
25 T. Giovannini, S. Gómez and C. Cappelli, Modeling Raman Spectra in Complex Environments: From Solutions to

Surface-Enhanced Raman Scattering, *J. Phys. Chem. Lett.*, 2025, **16**(12), 3106–3121.
26 L. Rayleigh, XXXIV. On the transmission of light through an atmosphere containing small particles in suspension, and on the origin of the blue of the sky, *London, Edinburgh Dublin Phil. Mag. J. Sci.*, 1899, **47**(287), 375–384.
27 G. Mie, Beiträge zur Optik trüber Medien, speziell kolloidaler Metallösungen, *Ann. Phys.*, 1908, **330**(3), 377–445.
28 A. G. Shard, R. C. Schofield, and C. Minelli, Chapter 3.2.3 - Ultraviolet–visible spectrophotometry, in *Characterization of Nanoparticles*, ed. V.-D. Hodoroaba, W. E. S. Unger, and A. G. Shard, Elsevier, 2020, pp. 185–196.
29 P. Scott, *Miepython: Pure Python Calculation of Mie Scattering*. 2025.
30 G. Mie, Beiträge zur Optik trüber Medien, speziell kolloidaler Metallösungen, *Ann. Phys.*, 1908, **330**(3), 377–445.
31 Y. A. Akimov, Mie scattering theory: a review of physical features and limitations, *arXiv*, 2024, preprint, arXiv:2401.04146, DOI: 10.48550/arXiv.2401.04146.
32 C. F. Bohren and H. D .R., Absorption and Scattering by a Sphere, in *Absorption and Scattering of Light by Small Particles*, 1998, pp. 82–129.
33 S. Prahl, *miepython: Pure python Calculation of Mie Scattering*, 2025, Zenodo, DOI: 10.5281/zenodo.15514362.
34 J. Grand, B. Auguié and E. C. Le Ru, Correction to Combined Extinction and Absorption UV–Visible Spectroscopy as a Method for Revealing Shape Imperfections of Metallic Nanoparticles, *Anal. Chem.*, 2020, **92**(5), 4164.
35 A. Djorović, *et al.*, Extinction-to-Absorption Ratio for Sensitive Determination of the Size and Dielectric Function of Gold Nanoparticles, *ACS Nano*, 2020, **14**(12), 17597–17605.
36 D. Acharya, *et al.*, Theoretical prediction of absorbance spectra considering the particle size distribution using Mie theory and their comparison with the experimental UV–Vis spectra of synthesized nanoparticles, *Spectrosc. Lett.*, 2018, **51**(3), 139–143.
37 M. R. Pollard, *et al.*, Polymer Nanoparticle Identification and Concentration Measurement Using Fiber-Enhanced Raman Spectroscopy, *Chemosensors*, 2020, **8**(1), 21.
38 J. A. Yabagi, *et al.*, The effect of gamma irradiation on chemical, morphology and optical properties of polystyrene nanosphere at various exposure time, *IOP Conf. Ser.: Mater. Sci. Eng.*, 2018, **298**(1), 012004.
39 M. Mazilu, *et al.*, Optimal algorithm for fluorescence suppression of modulated Raman spectroscopy, *Opt. Express*, 2010, **18**(11), 11382–11395.
40 K. K. Chow, *et al.*, A Raman cell based on hollow core photonic crystal fiber for human breath analysis, *Med. Phys.*, 2014, **41**(9), 092701.
41 E. S. Jung, *et al.*, Quantitative Raman analysis of microplastics in water using peak area ratios for concentration determination, *npj Clean Water*, 2024, **7**(1), 104.
42 Y. Hu, *et al.*, Analysis of the Effect of Particle Size on Polymorphic Quantitation by Raman Spectroscopy, *Appl. Spectrosc.*, 2006, **60**(9), 977–984.
43 H. Wang, C. K. Mann and T. J. Vickers, Effect of Powder Properties on the Intensity of Raman Scattering by Crystalline Solids, *Appl. Spectrosc.*, 2002, **56**(12), 1538–1544.

